Particle-phase processing of α-pinene NO₃ secondary organic aerosol in the dark

David M. Bell[1][*], Cheng Wu[2], Amelie Bertrand[1], Emelie Graham[2], Janne Schoonbaert[1], Stamatios Giannoukos[1a], Urs Baltensperger[1], Andre S. H. Prevot[1], Ilona Riipinen[2], Imad El Haddad[1], and Claudia Mohr[2*]

[1] Paul Scherrer Institute, Laboratory of Atmospheric Chemistry, 5232 Villigen, Switzerland

[2] Department of Environmental Science, Stockholm University, Sweden

[a] Now at: ETH Zurich, Department of Chemistry and Applied Biosciences, 8093 Zurich, Switzerland

Correspondence to: David.Bell@psi.ch and Claudia.Mohr@aces.su.se

Abstract. The NO_3 radical represents a significant night-time oxidant present downstream of polluted environments. There are studies that investigated the formation of secondary organic aerosol (SOA) from NO_3 radicals focusing on yields, general composition, and hydrolysis of organonitrates. However, there is limited knowledge about how the composition of NO_3-derived SOA evolves as a result of particle phase reactions. Here, SOA was formed from the reaction of α-pinene with NO_3 radicals generated from N_2O_5, and the resulting SOA aged in the dark. The initial composition of NO_3-derived α-pinene SOA was slightly dependent upon the concentration of N_2O_5 injected (excess of NO_3 or excess of α-pinene), but was largely dominated by dimer dinitrates ($C_{20}H_{32}N_2O_{8-13}$). Oxidation reactions (e.g. $C_{20}H_{32}N_2O_8$ → $C_{20}H_{32}N_2O_9$ → $C_{20}H_{32}N_2O_{10}$ etc…) accounted for 60-70% of the particle phase reactions observed. Fragmentation reactions and dimer degradation pathways made up the remainder of the particle-phase processes occurring. The exact oxidant is not known, though suggestions are offered (e.g. N_2O_5, organic peroxides, or peroxy-nitrates). Hydrolysis of –ONO2 functional groups was not an important loss term during dark aging under the relative humidity conditions of our experiments (58 – 62%), and changes in the bulk organonitrate composition were likely driven by evaporation of highly nitrogenated molecules. Overall, 25-30% of the particle-phase composition changes as a function of particle-phase reactions during dark aging representing an important atmospheric aging pathway.

1 Introduction

Organic aerosol in the atmosphere can have important impacts on human health and climate (Jimenez et al., 2009). A substantial fraction of the organic aerosol is secondary aerosol, which is formed from reactions that lower the volatility of a molecule (Ziemann and Atkinson, 2012). One of the most prevalent families of molecules undergoing these oxidation reactions

to form secondary organic aerosol (SOA) are monoterpenes. Unlike isoprene, monoterpenes are emitted both during the day

30 and night (Pye et al., 2010). Because of the importance of monoterpenes at night, nocturnal oxidants (O_3 and NO_3) play an important role in their transformation in the atmosphere (Brown and Stutz, 2012). A field study in the southeastern United States found that ~50% of the total aerosol burden at night comes from NO_3 radical derived chemistry (Xu et al., 2015;Xu et al., 2014;Ayres et al., 2015;Lee et al., 2016). Other studies have shown the importance of nitrate chemistry in both urban and pristine areas with monoterpenes (Yan et al., 2016;Stefenelli et al., 2019;Huang et al., 2019;Kiendler-Scharr et al., 2016).

35 Although α-pinene is globally the most abundant monoterpene (Guenther et al., 2000), β-pinene has been the most studied of monoterpenes interacting with NO_3 radicals because of resulting high SOA yields (Takeuchi and Ng, 2019;Nah et al., 2016;Boyd et al., 2015) relative to α-pinene. β-pinene was estimated to be the precursor of up to ~20% of the total nighttime OA in the Southeastern US (Ayres et al., 2015). However, recent studies show that SOA formation from α-pinene + NO_3 is also possible (Romonosky et al., 2017;Takeuchi and Ng, 2019;Nah et al., 2016). In chamber studies, SOA from both α-pinene

40 and β-pinene + NO_3 contains a substantial fraction of dimers when the radical balance is dominated by RO_2 + NO_3 or RO_2 + RO_2 reactions (Takeuchi and Ng, 2019;Claflin and Ziemann, 2018), while monomers are the dominant products when RO_2 + HO_2 is the dominant pathway (Nah et al., 2016). When experiments were conducted in the dark, monoterpene + NO_3 products were shown to steadily evolve, with a steady change in O:C and N:C ratios reported by Nah et al. (2016). In Takeuchi and Ng (2019) ~9-17% of organo-nitrates from either α-pinene or β-pinene SOA hydrolyze at moderate relative humidities (~ 50%

45 RH). The studies of Nah et al. (2016) relied on acidic seeds, which could impact the particle phase aging (Riva et al., 2019), when compared to neutral seeds or homogeneously nucleated SOA. Alternatively, Claflin and Ziemann (2018) speculated about the importance of dimer formation within the particle-phase itself for β-pinene + NO_3 SOA. However, quantifying the absolute magnitude of the importance of the particle-phase processes was not possible in any of these studies. These contrasting studies demonstrate the processes occurring during dark aging of NO_3 derived SOA are still not well understood, and warrants

50 further studies to improve our knowledge on the processes occurring during dark aging of NO_3 derived SOA.

The ability to observe the chemical changes in real time during aging have been limited to instruments with significant fragmentation, low time resolution, or limited to off-line analysis. The advent of new soft-ionization techniques makes it possible to follow these changes in real-time with high molecular resolution (Pospisilova et al., 2020). We will employ the

extractive electrospray ionization time-of-flight mass spectrometer (EESI-TOF) along with a chemical ionization mass spectrometer with filter inlet for gases and aerosols (FIGAERO-CIMS) to elucidate the particle-phase composition with high chemical and temporal resolution and uncover the changes occurring therein. Here, we investigate the composition of SOA formed from α-pinene + NO_3 in dark conditions, determine the processes occurring in the particle phase, separate them from products formed in the gas phase, and determine the magnitude of the effect dark aging has on the composition of NO_3 derived α-pinene SOA.

2. Experimental

2.1 Chamber Conditions

A series of batch-mode chamber experiments (Table 1) investigating formation and aging of SOA formed from NO_3-initiated chemistry was performed in the 8 m^3 Teflon chamber at the Paul Scherrer Institute, Switzerland, described previously (Platt et al., 2013). Measurements were performed with a proton-transfer-reaction with a quadrupole mass spectrometer (PTR-MS, Ionicon), extractive electrospray inlet coupled to a long time-of-flight mass spectrometer (EESI-ToF, Tofwerk), a scanning mobility particle sizer (SMPS, TSI model 3938), a chemical ionization mass spectrometer with filter inlet for gases and aerosols (FIGAERO-CIMS, Aerodyne), a thermo-denuder coupled with an SMPS, an ozone gas monitor (Thermo 49C), and a NO_x monitor (Thermo 42C). A zero air generator (AADCO) was used to supply clean air to the chamber and instrumentation. Isothermal evaporation chambers were used for the investigation of particle volatility. The FIGAERO-CIMS sampled on its own dedicated line from the atmospheric simulation chamber with a flow rate of 5 L min^{-1}. Gas monitors and PTR-MS operated behind a heated (80 °C) 3 m stainless steel sampling line with a 5 s residence time. The particle instruments sampled from a 3 m stainless steel line with ~3 s residence time. The chamber was cleaned after every experiment and overnight by purging it with zero air (50 L min^{-1} input and 50 L min^{-1} output), and heating it to 30 °C. In the morning the chamber was expanded to its full volume with zero air. The chamber was deemed clean if the particulate concentrations overnight were less than 50 cm^{-3} and NO_x levels below 30 ppb. A persistent contamination of cresol (~1 ppb) was present in the chamber from experiments that took place prior to those with α-pinene.

Five experiments generated α-pinene SOA from reactions with NO_3 radicals at 58 ± 5% relative humidity (RH) and 21 ± 3 °C. No seed particles were used in this study, in contrast to other studies that have been performed on similar systems

3

(Takeuchi and Ng, 2019). NO$_3$ radicals were formed from the decomposition of N$_2$O$_5$, which was injected by passing dry clean

80   air over a solid sample of N$_2$O$_5$. For blank experiments, α-pinene was injected ~30 min. after N$_2$O$_5$. In these experiments, no

new particles were formed after the N$_2$O$_5$ injection and prior to α-pinene injection; also the gaseous cresol contamination did

not lead to particle formation during blank experiments. However, in each experiment, the contamination was observed by

both the FIGAERO-CIMS and EESI-ToF after enough organic mass had formed to allow the contaminants to partition into

the particle phase; the cresol contamination constitute~1-2% of the total EESI-ToF signal and ~5% of the total FIGAERO

85   signal. In all experiments, new particle formation occurred promptly after injection of N$_2$O$_5$ when a VOC was present in the

chamber. α-pinene was injected volumetrically with the PTR-MS following the absolute concentration; in experiments 1 – 3,

~100 ppb of α-pinene were injected, and 20 ppb of α-pinene in Experiments 4 - 5. The FIGAERO-CIMS and EESI-ToF were

only present for experiments 1-3, which will be the focus of the discussion below. Even though the FIGAERO-CIMS and

EESI-ToF were not present for experiments 4 and 5, these experiments are included to confirm the changes in particle mass

90   concentration with dark aging at lower mass concentrations are consistent with the measurements at higher mass concentration.

The Framework for 0-D Atmospheric Modeling (F0AM) (Wolfe et al., 2016) with the Master Chemical Mechanism

(MCM) (Saunders et al., 2003;Jenkin et al., 1997) was used to model the gas-phase and radical chemistry in the chamber.

F0AM was used to estimate the amount of N$_2$O$_5$ injected into the chamber, and in all cases the concentration of N$_2$O$_5$ was

between 80 and 300 ppb. During dark aging (3-4 h) the volume of the chamber was reduced by instruments sampling from the

95   chamber, and no additional air was added to the chamber during this time.

100

Table 1) Experimental parameters for all experiments. [a]Measured by the SMPS, [b]modeled N_2O_5 concentration based on VOC decay assuming 1.2×10^{-12} sec^{-1} as the NO_3 + α-pinene rate constant, [c]volumetric addition of α-pinene.

Experiment #	Maximum SOA[a] (µg m^{-3})	N_2O_5[b] (ppb)	RH (%)	Temp	α-pinene injected[c] (ppb)	Particle Mass Spectrometers Operational
1	19	300	58	21	100	EESI (semi-operational) and FIGAERO-CIMS
2	39	80	60	22	100	EESI and FIGAERO-CIMS (first filter performed later)
3	62	300	58	18	100	EESI and FIGAERO-CIMS
4	8	400	58	20	20	-none-
5	7	200	62	20	20	-none-

105

In all experiments, the mass measured by the SMPS was corrected for particle wall loss. The wall loss rate (k_{wall}) was calculated from the exponential decay of the total particle number concentration (cm^{-3}) measured by the SMPS, corrected for coagulation. The particulate wall loss is defined by:

$$\frac{dN}{dt} = -k_{coag}N^2 - k_{wall}N \qquad \text{Eq 1.}$$

110 where N is the particle number concentration and k_{coag} corresponds to the coagulation coefficient (5E-10 s^{-1}). The number of particles lost during the measurement time was scaled according to the mean mass of the entire particle population, which is based on the geometric mean mobility diameter (d_m) from the measurement time, assuming a density of 1.2 g cm^{-3}. The wall loss-corrected mass was divided by the uncorrected mass to obtain the wall loss correction factor that was applied to the EESI-ToF and FIGAERO-CIMS data to correct for particle wall loss, during experiments 1-3.

115 **2.2 EESI-ToF – Extractive Electrospray Ionization Time-of-Flight Mass Spectrometer**

The EESI-ToF measured the molecular constituents of the SOA formed in the chamber, sampling the aerosols at 1 L min^{-1}. The aerosol sample passed through a multi-channel denuder that strips the gas phase species from the particles, with minimal evaporation of the particles (Lopez-Hilfiker et al., 2019). The aerosol sample intersected with a spray of droplets (50:50, H_2O : acetonitrile) doped with 100 ppm NaI which emanated from an electrospray probe. The soluble portion of the aerosol was

120　extracted into the liquid, and after the droplet evaporated, the molecules were observed in the mass spectrometer as Na^+-adducts. The adducts were guided through a series of ion-guides and are separated based on their mass-to-charge ratio in a time-of-flight mass spectrometer. In the experiments presented here, the resolution of the mass spectrometer was $5,500 – 7,000$. Background measurements were continually and repeatedly performed by sampling the contents of the atmospheric simulation chamber via a particulate filter (e.g. 4 min. chamber air without and 1 min. with filter). A noise filter was used to remove data

125　points impacted by severe electronic noise, which was periodically observed throughout the campaign. The reported signal was a result of subtracting the background filter periods from the adjacent sampling periods. A filtering threshold was applied to the EESI-ToF data, where signals that were 1σ (standard deviation) greater than background data were considered statistically significant and included in the analysis. The EESI-ToF time series were averaged to 5 min resolution, including one sample and filter period cycle. The EESI-ToF signal was scaled according to the molecular weight of each respective

130　molecule i and converted to a mass flow rate using:

$$EESI\ (ag\ s^{-1}) = \sum_i \frac{EESI(Hz)_i \cdot MW_i \cdot 10^{18}}{6.023E23}$$

where EESI(Hz) is the raw data from the TOF, and MW_i is the molecular weight, normalized using the Avogadro's number, and a conversion factor from grams to attograms. Within the EESI-ToF, the detection efficiency varied depending on a number of factors including particle size (Lee et al., 2021), extraction efficiency in the EESI-ToF droplet, and mass transmission of an

135　ion from the inlet to the mass spectrometer. Despite all these potential impacts, if all ions were measured equally, the overall agreement between measured EESI-ToF signal (attograms per second - ag s^{-1}) followed a linear trend with measured organic mass (SMPS) despite day-to-day variations in absolute intensity (Figure S2). Experiments 2 and 3 fell along the same slope, because the EESI-ToF capillary and TOF settings were not adjusted between experiments. In contrast, experiment 1 had a much lower slope because the EESI-ToF was still being optimized (capillary position and TOF settings were being altered)

140　and had low sensitivity during this experiment. Consequently, bulk information was obtained by long averaging times for experiment 1, but time series of individual molecular formulae was not used due to the noisy signal.

　　　　A majority of the ion signal (>95%) was from Na^+-adducts. However, a consequence of using acetonitrile (C_2H_3N) as a solvent, there was also a small fraction of the signal that is associated with Na^+-adducts+acetonitrile. For instance, Na^+-$C_{20}H_{32}N_2O_8$ was one of the main ions observed for α-pinene SOA, and there was an associated peak for Na^+-$C_{22}H_{35}N_3O_8$

145 $(C_{20}H_{32}N_2O_8 + C_2H_3N)$ that results from the interaction between spray solution and the constituent of SOA. For all $C_{20}H_{32}N_2O_x$ molecules, the acetonitrile cluster represented 1-3% of the parent ion. For the cases where unambiguous clustering occured (e.g. $C_{20} + C_2H_3N$), C_2H_3N was subtracted from the molecular formula. For some compounds, the molecular formulae of the clusters overlapped with C_{20} oxidation products (e.g. $C_{18}H_{28-32}N_{0-2}O_x$). As the C_{18} molecules represented less than 1% of the total signal, the possible contribution of the acetonitrile cluster was not corrected for. Because there was not a large variety in

150 the carbon distribution of the SOA formed, as shown in the results below, a majority of the mass was corrected for acetonitrile clustering.

One of the most prevalent peaks in the mass spectra of the EESI-ToF was the $C_{10}H_{16}O_2$ (~50-65% total signal), which resulted from an artefact of specific dimer degradation in the electrospray droplet. A follow-up paper will describe details the corrections for the artefact and our confidence in identifying it. In brief, the time series of the $C_{10}H_{16}O_2$ molecule was strongly

155 correlated ($R^2 > 0.96$) only with $C_{20}H_{32}N_2O_8$, shown in Fig. S1 (inset), even during evaporation experiments. Based on this correlation, $C_{20}H_{32}N_2O_8$ likely fragments in the electrospray droplet to form two $C_{10}H_{16}O_2$ species, which were observed, while the $-ONO_2$ groups were lost and not detected. If we presume two $C_{10}H_{16}O_2$ molecules come from a single $C_{20}H_{32}N_2O_8$ and correct the mass loss for the nitrate groups lost, then there is good agreement with the measured mass. Therefore, the total contribution of $C_{10}H_{16}O_2$ was converted to $C_{20}H_{32}N_2O_8$. Additional potential measurement artefacts included loss of HNO_3

160 (Liu et al., 2019), though, this was a minor pathway making up <1% of the parent ion signal for any molecular formula (e.g. $C_{20}H_{32}N_2O_x \rightarrow C_{20}H_{31}NO_{x-3} + HNO_3$).

2.3 FIGAERO-CIMS - Chemical ionization mass spectrometer with filter inlet for gases and aerosols

The molecular composition of organic compounds in gas and particle phases was measured using a FIGAERO-CIMS. The FIGAERO inlet was coupled with a high-resolution time-of-flight chemical-ionization mass spectrometer (HR-ToF-

165 CIMS) using I- as reagent ion and an X-ray generator as ion source. The resolution of the mass spectrometer was 5,000 – 6,000. The design and operation of the FIGAERO-CIMS were similar to that described in previous studies (Huang et al., 2019;Lopez-Hilfiker et al., 2014). Briefly, particles were collected on a 25mm Zefluor® PTFE filter (Pall Corp.) via a sampling port (flow rate 5 L min^{-1}). The duration of particle-phase sampling depended on the mass loadings and was 10 – 20 min for most of the experiments. During the particle-phase sampling, gases were directly measured by the CIMS from the chamber

170   via a Teflon line at 5 L min^{-1}. When the particle phase sampling was done, the gas-phase measurement was switched off and particles on the filter were desorbed by a flow of gradually heated ultra-high-purity (99.999 %) nitrogen and transported into the CIMS. A FIGAERO-CIMS desorption round lasted about 40 min: 20 min of ramping temperature of the nitrogen flow up to 200 $^{\circ}$C, followed by a 20 min "soak period" at a constant 200 $^{\circ}$C. After that it was cooled down to room temperature. The resulting mass spectral signal evolutions during a desorption round as a function of desorption temperature are called

175   thermograms (Lopez-Hilfiker et al., 2014). The raw FIGAERO-CIMS data were analysed with Tofware (Aerodyne Research, Inc. and Tofwerk AG) and codes written with MATLAB. The integration of thermograms of individual compounds yields their total signal in counts per deposition. For the first filter in Exp. 2, due to a software failure, the filter was stored wrapped in aluminum foil for ~7 h before the being desorbed. However, comparing the first filter with others, the changes in O/C, N/C as well as the ratio of monomers/dimers were similar to other experiments. For further details about the data analysis, see Wu

180   et al. (2021).

3 Results

3.1 Initial particle molecular composition and instrumental comparison

In the experiments performed here, the α-pinene rapidly reacts with NO$_3$, with corresponding prompt formation of organic aerosol mass measured by the SMPS (shown in Figure 1A). After α-pinene consumption and particle formation, the

185   SOA mass steadily decays by evaporation (Figure 1B), which is consistent with previous studies (Nah et al., 2016). In all experiments, except experiment 2, the α-pinene is fully consumed, while in experiment 2 there are ~20 ppb of unreacted α-pinene left over in the chamber after the N$_2$O$_5$ is fully consumed, because the injection of N$_2$O$_5$ was less than the other experiments. The incomplete consumption of α-pinene comes from a injection of N$_2$O$_5$ that was less than the total concentration of α-pinene. The relatively small concentrations of N$_2$O$_5$ injected also changes the radical balance in the chamber, which will

190   be discussed in the next section. In the other experiments with an excess of N$_2$O$_5$ injected, hydrolysis on the walls likely represents a significant sink for any unreacted N$_2$O$_5$. During the experiments presented here, the analysis will focus on the higher loading experiments (experiments 1-3) because both the FIGAERO-CIMS and EESI-ToF were not present for experiments 4 and 5 (see Table 1).

In this section we compare the chemical composition measured by both the EESI-ToF and FIGAERO-CIMS. Detailed mass spectra averaged from experiments 1 – 3 for both the EESI-ToF and FIGAERO-CIMS are presented in Figures 2A and B over the first 10-46 min after particle formation. Figure 2A also colors the composition according to the number of carbon atoms in the molecular formulae. Dinitrates dominate the dimer fraction of α-pinene SOA, with molecular formulae of $C_{20}H_{32}N_2O_{8-13}$ making up ~60 – 85% of the total composition for the EESI-ToF and 45 – 56% for the FIGAERO-CIMS (the range of values comes from the variation across experiments 1 – 3 for the beginning of each experiment), consistent with previous observations (Takeuchi and Ng, 2019), and with dominant $RO_2 + RO_2$ reactions shown for other systems (Zhao et al., 2018;Molteni et al., 2019). There are slight differences when comparing the carbon number distribution observed by both the FIGAERO-CIMS and the EESI-ToF, shown in Figures 2C and D, reflected in the EESI-ToF detecting more dimers over monomers, when compared to the FIGAERO-CIMS. Additionally, singly nitrated monomers ($C_{10}H_{15}NO_{5-10}$) are observed by both instruments (5-7% EESI-ToF and 7-10% FIGAERO-CIMS), while monomer dinitrates ($C_{10}H_{14,16}N_2O_{7-11}$) are mostly only observed by the FIGAERO-CIMS and are slightly above background levels in the EESI-ToF for experiment 3. The monomer dinitrates have the highest concentrations in experiments 1 (10%) and 3 (12%), while they are substantially lower in experiment 2 (2%). Monomer dinitrates likely form via an $RO_2 + NO_2$ reaction to form peroxynitrate functional groups(Chan et al., 2010), which is speculated to form monomer trinitrates in the isoprene + NO_3 system (Zhao et al., 2020). The lack of their formation in experiment 2 agrees with the smaller concentrations of N_2O_5 injected, and corresponding smaller amount of NO_2 present. The main differences between the instruments come from the oxygen distribution of the dinitrate dimers ($C_{20}H_{32}N_2O_{8-13}$) where the most prevalent molecular formulae are with #O = 8 for the EESI-ToF and #O = 9 for the FIGAERO-CIMS, shown in Figures 3A and 3B. This is similar to differences observed between offline ESI and online FIGAERO-CIMS measurements for β-pinene SOA (Takeuchi and Ng, 2019;Claflin and Ziemann, 2018). As mentioned above, there is a small contamination from cresol (C_7H_8O) in the chamber, which shows itself in a series of C_7 and C_{17} molecules present in the mass spectra (in experiment 2: 6% in the FIGAERO-CIMS and 1% in the EESI-ToF). The contaminant molecule with the largest signal in both instruments is $C_{17}H_{26}N_2O_{11}$, from a dimer formed between a cresol monomer and an α-pinene monomer. The changes of the contaminants with dark aging time is relatively minor with respect to all other particle-phase components and therefore they are spectators during aging.

Overall, the composition generally agrees between both instruments very well, demonstrating relatively good overlap in the main molecular classes observed (dimer dinitrates and singly nitrated monomers) making up ~65-90% of the total SOA composition in both instruments. Observed differences do not affect the general scope of the paper focused on the intra-particle reactions of organonitrate species, as will be shown in the following sections.

3.2 Gas-Phase Radical Chemistry and Impact on Particle Composition

Because particle-phase reactions are not well understood, it is necessary to understand what radical pathways controls the initial composition of the SOA. The radical chemistry of NO_3 is important to consider, because Ng et al. (2008) demonstrated that the balance of NO_3 and RO_2 radical chemistry plays an important role in the yields of formation of SOA from isoprene + NO_3. In their study, larger SOA yields were observed under an $RO_2 + RO_2$ dominant regime compared to an $RO_2 + NO_3$ dominant regime. The RO_2 chemistry regime promotes the formation of dimers with lower volatility increasing yields of SOA, and is consistent with the large prevalence of ROOR dimers observed in isoprene + NO_3 SOA (Ng et al., 2008). For monoterpenes, only minor differences were found in the yields of β-pinene + NO_3 between the $RO_2 + NO_3$ vs. $RO_2 + HO_2$ regimes, however, the $RO_2 + RO_2$ dominant regime was not investigated (Boyd et al., 2015).

F0AM was used here to model the fate of RO_2 radicals assuming generalized rate constants for the known RO_2 radicals formed via the reaction of α-pinene + NO_3. The MCM does not include intra-molecular hydrogen shifts, auto-oxidation reactions, nor ROOR formation, but despite these limitations, the MCM provides general insight into the predicted radical chemistry regimes. Based on the modelling, shown in Figure S3, $RO_2 + NO_3$ reactions are predicted to be the dominant pathway in the excess of N_2O_5 (experiments 1 and 3), while in the excess of α-pinene, $RO_2 + RO_2$ reactions will dominate (experiment 2). HO_2 is not an important reaction partner since there are limited formation mechanisms under our conditions (Boyd et al., 2015).

The first generation RO_2 radical from the reaction of α-pinene + NO_3 is $C_{10}H_{16}NO_5$, which can react with itself via the ROOR pathway and form $C_{20}H_{32}N_2O_8 + O_2$. Based on this reaction pathway the $C_{20}H_{32}N_2O_8$ likely contains two –ONO_2 functional groups and a peroxy linkage. This molecule is also the dominant dimer that is observed in the gas-phase at the beginning of the experiment, shown in Figure 3C, and observed by both instruments in the particle-phase. More oxygenated dimers ($C_{20}H_{32}N_2O_{9,10}$) are also observed in the gas-phase (Figure 3C), presumably arising from a similar dimer formation

mechanism ($RO_2 + RO_2$), but with more highly oxygenated RO_2 radicals that can form from the initial RO_2 through autooxidation (Bianchi et al., 2019) or the alkoxy pathway (Molteni et al., 2019). Highly oxygenated dinitrate C_{20} molecules detected here have also been observed in the gas-phase in pristine environments (Yan et al., 2016). Gas-phase measurements of $C_{20}H_{32}N_2O_{8-10}$ in Figure 3C importantly show the presence of dimers in the gas phase, demonstrating they are not exclusively formed in the particle phase, as hypothesized for β-pinene + NO_3 (Claflin and Ziemann, 2018).

Since we are operating in different predicted radical regimes, $RO_2 + NO_3$ dominated (experiments 1 & 3), and $RO_2 + RO_2$ dominated (experiment 2), there should be differences in the molecules that are observed in the respective experiments. In experiment 2 ($RO_2 + RO_2$ dominant), there is a larger fraction of dimers measured by both instruments (Figures 2C and 2D), in comparison to the other experiments (1 and 3) where $RO_2 + NO_3$ reactions are predicted to be the dominant pathway. Consistent with this observation, when dimer formation is suppressed (experiments 1 and 3) the monomer fraction has a contribution of 17-30% compared to 5-7% in experiment 2. Given the dominant fraction of dimers in all experiments, the importance of $RO_2 + RO_2$ reactions is underestimated, and the $RO_2 + NO_3$ reactivity is overestimated by the MCM, especially in experiments 1 and 3 (see Fig. S3). Despite the potential differences in the predicted radical regime, formation of dimers dominates the particle-phase composition, meaning $RO_2 + RO_2$ reactions are always very important even in experiments where $RO_2 + NO_3$ is predicted to be the dominant pathway. These findings are consistent with the importance of dimers formed from $RO_2 + RO_2$ reactions in other systems (Berndt et al., 2018a;Berndt et al., 2018b;Zhao et al., 2018;Ng et al., 2008;Molteni et al., 2019;Rissanen et al., 2015;Simon et al., 2020;Heinritzi et al., 2020), and with higher SOA yields from NO_3 initiated oxidation during dominant $RO_2 + RO_2$ chemistry (Ng et al., 2008;Bates et al., 2021).

3.3 Evolution in the Particle Phase Composition

Figure 1B shows that after formation of SOA the particles steadily evaporate in the chamber, suggesting subsequent changes in composition occurs via particle evaporation and/or other particle phase processes. The high time-resolution and detailed molecular information determined by the EESI-ToF, and the FIGAERO-CIMS, were used to determine the processes occurring and their time scales.

A comparison of the temporal evolution of the elemental N:C vs. O:C ratios for experiments 1-3 from EESI-ToF data is illustrated in Figure 4A, colored according to experimental time. Results from experiment 1 are noisy due to the low

sensitivity (see Figure S2), but the data is included because of the similar trend with the other experiments. The FIGAERO-CIMS is not included because of the low time resolution, which would include only 2 or 3 data points. In Figure 4A, there is a trend toward increasing O:C during the experiment, coupled with a decreasing N:C that correlates with mass concentration.

Considering each nitrogen atom is likely part of an –ONO_2 functional group (Takeuchi and Ng, 2019), the decrease in N:C suggests the increase in oxidation state (O:C) as a function of aging is larger than the apparent change shown in Figure 4A. Accounting for the substantial fraction of oxygen in the –ONO_2 functional groups, the O:C ratio for the non-nitrate functional group portion is determined by: $\#O_{No\text{-}Nitrogen} = \#O_{measured} - 3*\#N_{measured}$. With the contribution of the nitrate functional groups removed the O:C ratio (shown in Figure 4B) increases by 25-60% during the course of dark aging, demonstrating the components of SOA either undergo further oxidation during dark aging, or the particles´ O:C increases as a function of evaporation of compounds with lower O:C ratios from the particles.

If evaporation was the sole reason for changes in the oxidation state of the SOA, then there should be limited changes in the chemical composition as a function of aging except for those associated with evaporation (i.e. there should be nothing forming in the particle phase). Dimer dinitrates ($C_{20}H_{32}N_2O_{8\text{-}13}$) make up between 45 - 85% of the total ion signal through the whole dark aging time period, and will be the focus of the initial discussion on particle-phase processing. The wall-loss corrected time series of all $C_{20}H_{32}N_2O_x$ molecules over the first 180 min of the experiment is shown in Figure 5A for experiment 2 (with a similar plot for experment 3 shown in Figure S4, experiment 1 is not included because of the high relative noise). All molecules exhibit prompt incorporation in SOA, followed by steady changes, with molecules both increasing and decreasing in intensity with time. The $\#O = 8$ molecule steadily decays after particle formation with a decay rate of 0.01 min^{-1}, while the $\#O = 9$ steadily increases by 80% over 3 hours. To illustrate the changes more clearly, Figure 5B shows the changes in the composition relative to t = 10 min after particle formation, when the maximum in particle mass is reached. The $\#O = 10 - 11$ dinitrates increase $150 - 450\%$ during 3 h of dark aging, the contribution of these molecular formulae is ~1% at the beginning of the experiment and increases to ~2-5% of the total EESI-ToF signal. The FIGAERO-CIMS observes qualitatively similar changes in the composition as a function of dark aging with the $C_{20}H_{32}N_2O_{8\text{-}13}$ molecules, though the magnitude of the changes is smaller than those shown in Figure 5A and B. Overall, Figure 5A and B demonstrates production of more highly oxygenated dinitrate dimers in the particle phase. The production observed in experiment 2 is also observed in experiment 3, meaning it

occurs regardless of the presence of excess NO_3. Therefore, the particle-phase production is not due to gas-phase oxidation

295 reactions with excess NO_3 and subsequent condensation to the particle phase, but it must be occurring in the particle-phase.

Since we ruled out gas-phase reactions, production of higher oxygenated dimers could result either from monomer

conversion to dimers, or further oxidation in the particle phase. Figures 6A and 6B compare the carbon distribution of both the

EESI-ToF and FIGAERO-CIMS and how they change as a function of dark aging for experiment 3. This experiment is used

because there is the best overlap between the instruments (experiment 1 is also provided in Figure S5). In both the EESI-ToF

300 and FIGAERO-CIMS, the main species decaying in the particle phase are C_{20} dimers with additional contribution from the

decays of C_{10} molecules. Formation is dominated by other C_{20} molecules and some C_{10} molecules, with both instruments

showing the formation of more highly oxygenated C_{20} molecules (Figure 6C and 6D). The steady evaporation and lack of

oxidant in the gas phase likely precludes heterogeneous dimer formation from further gas-particle conversion. We cannot rule

out the possibility that dimers decay to monomers, and then undergo dimerization reactions to reform as higher oxygenated

305 dimers. Though, if the pathway to more highly oxygenated dimers occurred via degradation of dimers to monomers with

subsequent dimer formation, then there would be a shift to less oxygenated monomers to compensate this effect. The oxygen

distribution of the C_{10} molecules for the EESI-ToF is shown as a function of formation and depletion in the supplement and

they do not present a coherent change with dark aging (Figure S6).

The argument from the preceding paragraph assumes that the sensitivity of the EESI-ToF holds equally for all

310 molecules. On a molecule-by-molecule basis there is roughly a spread of 1 order of magnitude in the sensitivity of the EESI-

ToF toward different ions (Wang et al., 2021;Lopez-Hilfiker et al., 2019), but when comparing bulk SOA composition there

is good agreement with measured mass here (Fig. S2) and during measurements performed in Zurich, Switzerland (Qi et al.,

2019;Stefenelli et al., 2019). Additionally, the SOA composition measured by the EESI-ToF compares well to the predicted

particle composition based on gas-particle partitioning, using gas-phase measurements performed by the PTR3 (Surdu et al.,

315 2021). This provides confidence that the EESI-ToF is not missing specific molecules here. However, even if the EESI-ToF

were not sensitive to the species that are forming the more highly oxygenated molecules (i.e. monomer exchange reactions),

then the formation of higher oxygenated dimers ($C_{20}H_{32}N_2O_{9-11}$) would have to be nearly equally balanced by the consumption

/ disappearance of $C_{20}H_{32}N_2O_8$ (in order for the SMPS mass and EESI to agree in Fig. S2). Further, the FIGAERO-CIMS

would have to be biased in the exact same way as the EESI-ToF. Considering the agreement presented here and in previous studies it is more likely that the combination of the EESI and FIGAERO are capturing the change in chemical composition.

Therefore, the species initially formed in the gas-phase appear to undergo particle-phase oxidation to form more highly oxygenated molecules observed in Figures 5 and 6. The other important particle-phase reaction pathways shown in Figure 6 include fragmentation reactions (e.g. $C_{20} \rightarrow C_{19}$) and dimer degradation to monomers, which will be discussed further in terms of their absolute magnitude in the follow section.

3.4 Absolute Magnitude of Particle-Phase Reactions

Using Figures 5 and 6 it is possible to assess the magnitude of the processes taking place in the particle phase by taking all molecules observed by the EESI-ToF that are formed relative to $t = 10$ min and creating a mass balance during the whole dark aging period. Figure 7 shows the absolute intensity of all molecules detected by the EESI-ToF from experiment 2, highlighting the fraction of molecules increasing after the maximum in the organic mass concentration (shown in light blue), the signal of those molecular formulae that decrease (in orange, of which $C_{20}H_{32}N_2O_8$ makes up the great majority), and the initial contribution of the molecules that increase (dark blue). The molecules formed during the dark aging period make up ~30% of the total aerosol composition after 3 hours, representing a significant shift in the composition of SOA from the initially formed species. The formation found in the particle phase for experiment 3 is ~25% (shown in Figure S7), and is similar to that reported in Figure 7. If there was formation of volatile species, then this would not be captured by the current treatment and the magnitude of particle-phase processes would be even larger. Therefore, the reported 25-30% formation via particle-phase processes would be closer to 50% if evaporation was resulting from particle-phase reactions and not solely from volatile components repartitioning. Additionally, this treatment also does not account for potential step-wise oxidation reactions (e.g. $C_{20}H_{32}N_2O_8 \rightarrow C_{20}H_{32}N_2O_9 \rightarrow C_{20}H_{32}N_2O_{10}$), which would again result in an underestimate of the importance of particle-phase reactions. Therefore, a lower estimate of 25 – 30% of the total composition of α-pinene SOA is altered as a function of particle-phase processes over the 3-hour experimental time.

Figures 7 and S7 also show that particle-phase processes appear to be the most important over the first 2-2.5 hours of dark aging. Nearly all of the changes in the particle composition observed by the EESI-ToF come at the expense of $C_{20}H_{32}N_2O_8$, which diminishes from 70% of the total composition to ~35% after 3 hours of aging. Assuming the steady formation of higher

14

oxidation products is the result of a reaction with $C_{20}H_{32}N_2O_8$, the summation of signal forming after $t = 10$ min in Figure 5A

345   represents the fraction of $C_{20}H_{32}N_2O_8$ consumed via particle-phase processes. In experiment 2, the $C_{20}H_{32}N_2O_8$ has a mass flux

of 1.05 ag s^{-1} and it decreases to 0.61 ag s^{-1} after 3 hours, with a corresponding increase of oxidation products from 0.17 ag s^{-1} to 0.38 ag s^{-1} over that same time frame (shown in Figure 5A). Approximately half of the total depletion observed arises from

an increase in oxidation, with the remainder coming from evaporative losses.

Although oxidation reactions account for a large majority of the particle-phase processes occurring, Figure 6A-D

350   shows it is not the only process occurring. The increases in the oxidation state of the C_{20} dimers make up 60-70% (range for

experiments 2 and 3) of the total fraction of the species formed in the particle phase. Using analysis similar to the results shown

in Figure 6A-D, we can separate the other processes according to how the carbon distribution changes. The other two minor

pathways observed by the EESI-ToF are: increases in the monomer fraction (10-15% to the total changes), and formation of

$C_{8,9}$ or $C_{18,19}$ via fragmentation reactions from C_{10} or C_{20} molecules (10-20%). Fragmentation reactions will also lead to the

355   formation of smaller molecules containing 1-2 carbon atoms, which should rapidly evaporate from the particle phase.

Assuming the molecules leaving the particle phase have a molecular formula of CH_2O, as a simple example, it would represent

~10% loss of mass relative to $C_{20}H_{32}N_2O_8$. The amount of mass evaporating from the particle from fragmentation reactions

would be on the order of 0.2 – 0.3% of the total mass (or 0.1 µg m^{-3} in the experiment shown in Figure 8). Therefore,

fragmentation reactions are not responsible for a significant loss of mass during dark aging. We should note, we do observe a

360   few molecules increasing more than 25% in the gas-phase consistent with fragmentation reactions, including: $C_2H_4O_3$, $C_3H_6O_3$,

$C_4H_8O_3$, $C_3H_5NO_5$, $C_4H_7NO_5$, $C_5H_9NO_5$.

In Figure 4A we show the N:C ratio decreases during dark aging. Removal of dimer dinitrates results in a significant

mass change during the dark aging period (10 – 30% of the total signal). Due to the significant nitrogen content of these

dinitrate dimers, they will significantly impact the N:C ratio during aging. Figure 1b shows that the SOA evaporates during

365   aging in the chamber. Evaporative loss of dinitrate dimers is possible, though not common considering dimers typically have

very low volatility. However, when performing isothermal evaporation measurements in the atmospheric simulation chamber

both the $C_{20}H_{32}N_2O_{8,9}$ are susceptible to repartitioning (Figure S8). Because these dimers are low-volatility to semi-volatile

molecules they are in equilibrium between the particles, gas-phase, and the walls (Bertrand et al., 2018;Krechmer et al., 2020).

15

Therefore, part of the loss of $C_{20}H_{32}N_2O_{8,9}$ is due to repartitioning and accounts for a significant fraction of the organonitrates lost from the particle phase observed by the EESI-ToF, and a significant fraction of the decreasing signal in the FIGAERO-CIMS. Previously, the loss of NO_3 from the particle phase has been assumed to come from hydrolysis of $-ONO_2$ functional groups due to the loss of NO_3 measured by the AMS (Takeuchi and Ng, 2019;Nah et al., 2016). Here, the hydrolysis products ($C_{20}H_{33}NO_{6-12}$) make up less than 1% of their corresponding dinitrate species $C_{20}H_{32}N_2O_{8-14}$, demonstrating that hydrolysis of the main dinitrate dimers is not a significant loss term for this system. The lack of hydrolysis could come from the lack of water in the particles, which could differ from other experiments that have used seed aerosols (Takeuchi and Ng, 2019; Nah et al., 2016).

3.5 Possible Oxidation Pathways

In order to have oxidation reactions occurring in the particle-phase, such as the observed $C_{20}H_{32}N_2O_8$ to $C_{20}H_{32}N_2O_9$ conversion, there needs to be an oxidant or radical present with which to react. Radicals may act as oxidants through hydrogen abstraction reactions, with subsequent O_2 addition to the molecule that has lost a hydrogen. This would be a chemical pathway to form higher oxygenated molecules, and is analogous to similar reactions occurring in the gas phase (Molteni et al., 2019;Bianchi et al., 2019;Molteni et al., 2018). However, these reactions are not well-established in the particle-phase. Below, we speculate about some potential pathways and sources of radicals in the particle-phase.

Radical chemistry could be initiated from organic peroxides or peroxy nitrates incorporated in the particle phase, initiated from the scission of O-O bonds in organic peroxides. Considering the peroxy nitrate content is controlled by the concentration of NO_2 we would expect that this would only be important for experiments 1 and 3, and not for experiment 2. Because the magnitude of oxidation is similar between experiments 2 and 3, peroxy nitrates are likely not an important source of radicals. Degradation of dimers with a peroxy linkage could be prone to this effect, which would likely affect those species formed in the gas phase, $C_{20}H_{32}N_2O_{8-10}$, and these molecules are also abundant in all experiments. For the higher oxygenated molecules ($C_{20}H_{32}N_2O_{9,10}$), this effect would be obscured by the formation that dominates their time series, while for $C_{20}H_{32}N_2O_8$ to disentangle this effect from evaporation becomes difficult.

The FIGAERO-CIMS also observes a small fraction (<0.1 µg m^{-3}) of N_2O_5 present in the particle phase, which could act as an oxidant. The fraction of N_2O_5 in the particle phase decreases with time during the experiment (~50% over ~3 hours)

(shown in Figure S7), indicating it is being consumed or evaporating from the particle phase. Though, N_2O_5 is present in the

395   particle phase in experiments both with and without excess of N_2O_5, which is surprising considering its high volatility.

Overall, N_2O_5 present in the particle phase or organic peroxides could be responsible for the continued oxidation in the particle phase. However, in the system presented here, we are unable to assess which potential oxidant or reaction is more important because each oxidant will likely result in a similar reaction scheme and similar products.

4 Conclusions and Atmospheric Implications

400   The composition of NO_3-derived α-pinene SOA is dominated by dimers formed through RO_2-RO_2 reactions under the experiment conditions in this study. Pye et al. (2015) modeled the atmospheric conditions during nighttime chemistry in the southeastern US showing that the reactivity of RO_2 radicals in the atmosphere will react with either other RO_2 radicals (~40%) or HO_2 radicals (60%), with little reactivity with NO_3 radicals. In pristine areas, the termination of RO_2 radicals can be dominated by reactions with other RO_2's (Yan et al., 2016). Given the prevalence of dimers formed from NO_3 chemistry

405   (regardless of the concentration of NO_3 radicals), as shown in our study, they will be atmospherically important and form in most environments due to the relatively fast reaction rates between RO_2 radicals. These results illustrate that after formation in the gas phase, dimers will condense to the particle phase where further reactions will proceed. Oxidation reactions are the dominant reaction pathway accounting for 60-70% of the change in composition, while fragmentation (~10-20%) and dimer decay to monomers (10-15%) are the minor pathways. Although there are changes in the nitrogen content, they do not appear

410   to be associated with hydrolysis of nitrate functional groups, but rather the repartitioning of low-volatility/semi-volatile highly nitrated molecules. An open question remains the source of oxidation in the particle phase, as it could come from the degradation of organic peroxides or from the small amount of N_2O_5 present. Despite not knowing the source of oxidation, the results presented here, along with those shown for α-pinene derived SOA (from O_3) (Pospisilova et al., 2020;D'Ambro et al., 2018), demonstrate that SOA for both NO_3 or O_3, two of the major oxidants in the atmosphere, steadily evolves in the dark

415   without external stimuli.

Performing the experiments in a way to balance the radical chemistry, via the addition of HO_2, would be ideal to replicate atmospheric chemistry accurately depending on the region. The results presented here are clearly tilted toward RO_2 – RO_2 reactions or RO_2-NO_3 reactions. The presence of HO_2 radicals will promote the formation of monomer hydroperoxide

containing molecules over dimers, which will impact the ability to form lower volatility dimers, and increase the prevalence

420   of hydroperoxide functional groups. The presence of hydroperoxide functional groups could promote particle-phase reactions if the peroxide groups are able to degrade and act as a source of radicals in the particle phase. Overall, particle-phase processing of NO_3 derived SOA is likely important regardless of the radical regime, since $RO_2 + RO_2$ dimer formation is always an important sink of RO_2 radicals.

       The overall effect of chemical aging of NO_3 derived SOA in the dark will be towards less volatile particles as a

425   function of residence time in the atmosphere. The extent of the oxidation and aging in the particle phase could continue as long as there is a source of oxidant present. The reactions taking place in the particle phase result in changes of 25-30% (lower estimate) of the composition of NO_3 derived SOA. The particle-phase reactions slow / cease after 3 hours. In the atmosphere there will be continual production and partitioning of oxidation products, which could continue this process throughout the night.

430   The atmospheric consequence of these results is that we will typically over-predict the volatility of NO_3-derived SOA when aging reactions are not included, under-predict its impact on the lifetime of SOA in the atmosphere, and under-predict the lifetime of organonitrates in the atmosphere. Investigating the detailed chemistry of NO_3-derived SOA as a function of relative humidity would provide further insight to assess the potential role of hydrolysis of nitrate functional groups, and its impact on these particle-phase processes.

435   **Data Availability**

The datasets are available upon request from the correspond authors. Chamber data will available upon publication from: https://data.eurochamp.org/

Author Contributions

DMB, CW, CM designed the study. Chamber experiments were carried out by DMB, CW, ELG, AB, SG, CM. Data analysis

440   and interpretation was performed by DMB, CW, ELG, IR, JS, CM. DMB wrote the manuscript, with input from all co-authors. All co-authors read and commented on the manuscript.

Competing interests

The authors declare that they have no conflict of interest.

Acknowledgements

References

450   Ayres, B. R., Allen, H. M., Draper, D. C., Brown, S. S., Wild, R. J., Jimenez, J. L., Day, D. A., Campuzano-Jost, P., Hu, W., de Gouw, J., Koss, A., Cohen, R. C., Duffey, K. C., Romer, P., Baumann, K., Edgerton, E., Takahama, S., Thornton, J. A., Lee, B. H., Lopez-Hilfiker, F. D., Mohr, C., Wennberg, P. O., Nguyen, T. B., Teng, A., Goldstein, A. H., Olson, K., and Fry, J. L.: Organic nitrate aerosol formation via NO_3 + biogenic volatile organic compounds in the southeastern United States, Atmos. Chem. Phys., 15, 13377-13392, 10.5194/acp-15-13377-2015, 2015.

455   Bates, K. H., Burke, G. J. P., Cope, J. D., and Nguyen, T. B.: The nitrate radical (NO3) oxidation of alpha-pinene is a significant source of secondary organic aerosol and organic nitrogen under simulated ambient nighttime conditions, Atmos. Chem. Phys. Discuss., 2021, 1-24, 10.5194/acp-2021-703, 2021.

Berndt, T., Mentler, B., Scholz, W., Fischer, L., Herrmann, H., Kulmala, M., and Hansel, A.: Accretion Product Formation from Ozonolysis and OH Radical Reaction of α-Pinene: Mechanistic Insight and the Influence of Isoprene and Ethylene, Environmental Science & 460   Technology, 52, 11069-11077, 10.1021/acs.est.8b02210, 2018a.

Berndt, T., Scholz, W., Mentler, B., Fischer, L., Herrmann, H., Kulmala, M., and Hansel, A.: Accretion Product Formation from Self- and Cross-Reactions of RO2 Radicals in the Atmosphere, Angewandte Chemie International Edition, 57, 3820-3824, 10.1002/anie.201710989, 2018b.

Bertrand, A., Stefenelli, G., Pieber, S. M., Bruns, E. A., Temime-Roussel, B., Slowik, J. G., Wortham, H., Prévôt, A. S. H., El Haddad, I., 465   and Marchand, N.: Influence of the vapor wall loss on the degradation rate constants in chamber experiments of levoglucosan and other biomass burning markers, Atmos. Chem. Phys., 18, 10915-10930, 10.5194/acp-18-10915-2018, 2018.

Bianchi, F., Kurtén, T., Riva, M., Mohr, C., Rissanen, M. P., Roldin, P., Berndt, T., Crounse, J. D., Wennberg, P. O., Mentel, T. F., Wildt, J., Junninen, H., Jokinen, T., Kulmala, M., Worsnop, D. R., Thornton, J. A., Donahue, N., Kjaergaard, H. G., and Ehn, M.: Highly Oxygenated Organic Molecules (HOM) from Gas-Phase Autoxidation Involving Peroxy Radicals: A Key Contributor to Atmospheric 470   Aerosol, Chemical Reviews, 119, 3472-3509, 10.1021/acs.chemrev.8b00395, 2019.

Boyd, C. M., Sanchez, J., Xu, L., Eugene, A. J., Nah, T., Tuet, W. Y., Guzman, M. I., and Ng, N. L.: Secondary organic aerosol formation from the β-pinene+NO_3 system: effect of humidity and peroxy radical fate, Atmos. Chem. Phys., 15, 7497-7522, 10.5194/acp-15-7497-2015, 2015.

Brown, S. S., and Stutz, J.: Nighttime radical observations and chemistry, Chemical Society Reviews, 41, 6405-6447, 10.1039/C2CS35181A, 475   2012.

Chan, A. W. H., Chan, M. N., Surratt, J. D., Chhabra, P. S., Loza, C. L., Crounse, J. D., Yee, L. D., Flagan, R. C., Wennberg, P. O., and Seinfeld, J. H.: Role of aldehyde chemistry and NO_x concentrations in secondary organic aerosol formation, Atmos. Chem. Phys., 10, 7169-7188, 10.5194/acp-10-7169-2010, 2010.

480 Claflin, M. S., and Ziemann, P. J.: Identification and Quantitation of Aerosol Products of the Reaction of β-Pinene with NO3 Radicals and Implications for Gas- and Particle-Phase Reaction Mechanisms, The Journal of Physical Chemistry A, 122, 3640-3652, 10.1021/acs.jpca.8b00692, 2018.

D'Ambro, E. L., Schobesberger, S., Zaveri, R. A., Shilling, J. E., Lee, B. H., Lopez-Hilfiker, F. D., Mohr, C., and Thornton, J. A.: Isothermal Evaporation of α-Pinene Ozonolysis SOA: Volatility, Phase State, and Oligomeric Composition, ACS Earth and Space Chemistry, 2, 1058-1067, 10.1021/acsearthspacechem.8b00084, 2018.

485 Guenther, A., Geron, C., Pierce, T., Lamb, B., Harley, P., and Fall, R.: Natural emissions of non-methane volatile organic compounds, carbon monoxide, and oxides of nitrogen from North America, Atmospheric Environment, 34, 2205-2230, https://doi.org/10.1016/S1352-2310(99)00465-3, 2000.

Heinritzi, M., Dada, L., Simon, M., Stolzenburg, D., Wagner, A. C., Fischer, L., Ahonen, L. R., Amanatidis, S., Baalbaki, R., Baccarini, A., Bauer, P. S., Baumgartner, B., Bianchi, F., Brilke, S., Chen, D., Chiu, R., Dias, A., Dommen, J., Duplissy, J., Finkenzeller, H., Frege, C.,
490 Fuchs, C., Garmash, O., Gordon, H., Granzin, M., El Haddad, I., He, X., Helm, J., Hofbauer, V., Hoyle, C. R., Kangasluoma, J., Keber, T., Kim, C., Kürten, A., Lamkaddam, H., Laurila, T. M., Lampilahti, J., Lee, C. P., Lehtipalo, K., Leiminger, M., Mai, H., Makhmutov, V., Manninen, H. E., Marten, R., Mathot, S., Mauldin, R. L., Mentler, B., Molteni, U., Müller, T., Nie, W., Nieminen, T., Onnela, A., Partoll, E., Passananti, M., Petäjä, T., Pfeifer, J., Pospisilova, V., Quéléver, L. L. J., Rissanen, M. P., Rose, C., Schobesberger, S., Scholz, W., Scholze, K., Sipilä, M., Steiner, G., Stozhkov, Y., Tauber, C., Tham, Y. J., Vazquez-Pufleau, M., Virtanen, A., Vogel, A. L., Volkamer, R.,
495 Wagner, R., Wang, M., Weitz, L., Wimmer, D., Xiao, M., Yan, C., Ye, P., Zha, Q., Zhou, X., Amorim, A., Baltensperger, U., Hansel, A., Kulmala, M., Tomé, A., Winkler, P. M., Worsnop, D. R., Donahue, N. M., Kirkby, J., and Curtius, J.: Molecular understanding of the suppression of new-particle formation by isoprene, Atmos. Chem. Phys., 20, 11809-11821, 10.5194/acp-20-11809-2020, 2020.

Huang, W., Saathoff, H., Shen, X., Ramisetty, R., Leisner, T., and Mohr, C.: Chemical Characterization of Highly Functionalized Organonitrates Contributing to Night-Time Organic Aerosol Mass Loadings and Particle Growth, Environmental Science & Technology,
500 53, 1165-1174, 10.1021/acs.est.8b05826, 2019.

Jenkin, M. E., Saunders, S. M., and Pilling, M. J.: The tropospheric degradation of volatile organic compounds: a protocol for mechanism development, Atmospheric Environment, 31, 81-104, https://doi.org/10.1016/S1352-2310(96)00105-7, 1997.

Jimenez, J. L., Canagaratna, M. R., Donahue, N. M., Prevot, A. S., Zhang, Q., Kroll, J. H., DeCarlo, P. F., Allan, J. D., Coe, H., Ng, N. L., Aiken, A. C., Docherty, K. S., Ulbrich, I. M., Grieshop, A. P., Robinson, A. L., Duplissy, J., Smith, J. D., Wilson, K. R., Lanz, V. A.,
505 Hueglin, C., Sun, Y. L., Tian, J., Laaksonen, A., Raatikainen, T., Rautiainen, J., Vaattovaara, P., Ehn, M., Kulmala, M., Tomlinson, J. M., Collins, D. R., Cubison, M. J., Dunlea, E. J., Huffman, J. A., Onasch, T. B., Alfarra, M. R., Williams, P. I., Bower, K., Kondo, Y., Schneider, J., Drewnick, F., Borrmann, S., Weimer, S., Demerjian, K., Salcedo, D., Cottrell, L., Griffin, R., Takami, A., Miyoshi, T., Hatakeyama, S., Shimono, A., Sun, J. Y., Zhang, Y. M., Dzepina, K., Kimmel, J. R., Sueper, D., Jayne, J. T., Herndon, S. C., Trimborn, A. M., Williams, L. R., Wood, E. C., Middlebrook, A. M., Kolb, C. E., Baltensperger, U., and Worsnop, D. R.: Evolution of organic aerosols in the atmosphere,
510 Science, 326, 1525-1529, 10.1126/science.1180353, 2009.

Kiendler-Scharr, A., Mensah, A. A., Friese, E., Topping, D., Nemitz, E., Prevot, A. S. H., Äijälä, M., Allan, J., Canonaco, F., Canagaratna, M., Carbone, S., Crippa, M., Dall Osto, M., Day, D. A., De Carlo, P., Di Marco, C. F., Elbern, H., Eriksson, A., Freney, E., Hao, L., Herrmann, H., Hildebrandt, L., Hillamo, R., Jimenez, J. L., Laaksonen, A., McFiggans, G., Mohr, C., O'Dowd, C., Otjes, R., Ovadnevaite, J., Pandis, S. N., Poulain, L., Schlag, P., Sellegri, K., Swietlicki, E., Tiitta, P., Vermeulen, A., Wahner, A., Worsnop, D., and Wu, H. C.:
515 Ubiquity of organic nitrates from nighttime chemistry in the European submicron aerosol, Geophysical Research Letters, 43, 7735-7744, https://doi.org/10.1002/2016GL069239, 2016.

Krechmer, J. E., Day, D. A., and Jimenez, J. L.: Always Lost but Never Forgotten: Gas-Phase Wall Losses Are Important in All Teflon Environmental Chambers, Environmental Science & Technology, 54, 12890-12897, 10.1021/acs.est.0c03381, 2020.

Lee, B. H., Mohr, C., Lopez-Hilfiker, F. D., Lutz, A., Hallquist, M., Lee, L., Romer, P., Cohen, R. C., Iyer, S., Kurtén, T., Hu, W., Day, D.
520 A., Campuzano-Jost, P., Jimenez, J. L., Xu, L., Ng, N. L., Guo, H., Weber, R. J., Wild, R. J., Brown, S. S., Koss, A., de Gouw, J., Olson, K., Goldstein, A. H., Seco, R., Kim, S., McAvey, K., Shepson, P. B., Starn, T., Baumann, K., Edgerton, E. S., Liu, J., Shilling, J. E., Miller, D. O., Brune, W., Schobesberger, S., Ambro, E. L., and Thornton, J. A.: Highly functionalized organic nitrates in the southeast United States: Contribution to secondary organic aerosol and reactive nitrogen budgets, Proceedings of the National Academy of Sciences, 113, 1516, 10.1073/pnas.1508108113, 2016.

525   Lee, C. P., Surdu, M., Bell, D. M., Lamkaddam, H., Wang, M., Ataei, F., Hofbauer, V., Lopez, B., Donahue, N. M., Dommen, J., Prevot, A. S. H., Slowik, J. G., Wang, D., Baltensperger, U., and Haddad, I. E.: Effects of Aerosol Size and Coating Thickness on the Molecular Detection using Extractive Electrospray Ionization, Atmospheric Measurement Techniques submitted, 2021.

Liu, X., Day, D. A., Krechmer, J. E., Brown, W., Peng, Z., Ziemann, P. J., and Jimenez, J. L.: Direct measurements of semi-volatile organic compound dynamics show near-unity mass accommodation coefficients for diverse aerosols, Communications Chemistry, 2, 98,
530   10.1038/s42004-019-0200-x, 2019.

Lopez-Hilfiker, F. D., Mohr, C., Ehn, M., Rubach, F., Kleist, E., Wildt, J., Mentel, T. F., Lutz, A., Hallquist, M., Worsnop, D., and Thornton, J. A.: A novel method for online analysis of gas and particle composition: description and evaluation of a Filter Inlet for Gases and AEROsols (FIGAERO), Atmos. Meas. Tech., 7, 983-1001, 10.5194/amt-7-983-2014, 2014.

Lopez-Hilfiker, F. D., Pospisilova, V., Huang, W., Kalberer, M., Mohr, C., Stefenelli, G., Thornton, J. A., Baltensperger, U., Prevot, A. S.
535   H., and Slowik, J. G.: An extractive electrospray ionization time-of-flight mass spectrometer (EESI-TOF) for online measurement of atmospheric aerosol particles, Atmos. Meas. Tech., 12, 4867-4886, 10.5194/amt-12-4867-2019, 2019.

Molteni, U., Bianchi, F., Klein, F., El Haddad, I., Frege, C., Rossi, M. J., Dommen, J., and Baltensperger, U.: Formation of highly oxygenated organic molecules from aromatic compounds, Atmospheric Chemistry and Physics, 18, 1909-1921, 10.5194/acp-18-1909-2018, 2018.

Molteni, U., Simon, M., Heinritzi, M., Hoyle, C. R., Bernhammer, A.-K., Bianchi, F., Breitenlechner, M., Brilke, S., Dias, A., Duplissy, J.,
540   Frege, C., Gordon, H., Heyn, C., Jokinen, T., Kürten, A., Lehtipalo, K., Makhmutov, V., Petäjä, T., Pieber, S. M., Praplan, A. P., Schobesberger, S., Steiner, G., Stozhkov, Y., Tomé, A., Tröstl, J., Wagner, A. C., Wagner, R., Williamson, C., Yan, C., Baltensperger, U., Curtius, J., Donahue, N. M., Hansel, A., Kirkby, J., Kulmala, M., Worsnop, D. R., and Dommen, J.: Formation of highly oxygenated organic molecules from α-pinene ozonolysis: chemical characteristics, mechanism, and kinetic model development, ACS Earth Space Chem., 3, 873-883, 10.1021/acsearthspacechem.9b00035, 2019.

545   Nah, T., Sanchez, J., Boyd, C. M., and Ng, N. L.: Photochemical Aging of α-pinene and β-pinene Secondary Organic Aerosol formed from Nitrate Radical Oxidation, Environmental Science & Technology, 50, 222-231, 10.1021/acs.est.5b04594, 2016.

Ng, N. L., Kwan, A. J., Surratt, J. D., Chan, A. W. H., Chhabra, P. S., Sorooshian, A., Pye, H. O. T., Crounse, J. D., Wennberg, P. O., Flagan, R. C., and Seinfeld, J. H.: Secondary organic aerosol (SOA) formation from reaction of isoprene with nitrate radicals (NO$_3$), Atmos. Chem. Phys., 8, 4117-4140, 10.5194/acp-8-4117-2008, 2008.

550   Platt, S. M., El Haddad, I., Zardini, A. A., Clairotte, M., Astorga, C., Wolf, R., Slowik, J. G., Temime-Roussel, B., Marchand, N., Ježek, I., Drinovec, L., Močnik, G., Möhler, O., Richter, R., Barmet, P., Bianchi, F., Baltensperger, U., and Prévôt, A. S. H.: Secondary organic aerosol formation from gasoline vehicle emissions in a new mobile environmental reaction chamber, Atmospheric Chemistry and Physics, 13, 9141-9158, 10.5194/acp-13-9141-2013, 2013.

Pospisilova, V., Lopez-Hilfiker, F. D., Bell, D. M., El Haddad, I., Mohr, C., Huang, W., Heikkinen, L., Xiao, M., Dommen, J., Prevot, A. S.
555   H., Baltensperger, U., and Slowik, J. G.: On the fate of oxygenated organic molecules in atmospheric aerosol particles, Sci. Adv., 6, eaax8922, 10.1126/sciadv.aax8922, 2020.

Pye, H. O. T., Chan, A. W. H., Barkley, M. P., and Seinfeld, J. H.: Global modeling of organic aerosol: the importance of reactive nitrogen (NO$_x$ and NO$_3$), Atmos. Chem. Phys., 10, 11261-11276, 10.5194/acp-10-11261-2010, 2010.

Pye, H. O. T., Luecken, D. J., Xu, L., Boyd, C. M., Ng, N. L., Baker, K. R., Ayres, B. R., Bash, J. O., Baumann, K., Carter, W. P. L.,
560   Edgerton, E., Fry, J. L., Hutzell, W. T., Schwede, D. B., and Shepson, P. B.: Modeling the Current and Future Roles of Particulate Organic Nitrates in the Southeastern United States, Environmental Science & Technology, 49, 14195-14203, 10.1021/acs.est.5b03738, 2015.

Qi, L., Chen, M., Stefenelli, G., Pospisilova, V., Tong, Y., Bertrand, A., Hueglin, C., Ge, X., Baltensperger, U., Prévôt, A. S. H., and Slowik, J. G.: Organic aerosol source apportionment in Zurich using an extractive electrospray ionization time-of-flight mass spectrometer (EESI-TOF-MS) – Part 2: biomass burning influences in winter, Atmospheric Chemistry and Physics, 19, 8037-8062, 10.5194/acp-19-8037-2019,
565   2019.

Rissanen, M. P., Kurtén, T., Sipilä, M., Thornton, J. A., Kausiala, O., Garmash, O., Kjaergaard, H. G., Petäjä, T., Worsnop, D. R., Ehn, M., and Kulmala, M.: Effects of Chemical Complexity on the Autoxidation Mechanisms of Endocyclic Alkene Ozonolysis Products: From Methylcyclohexenes toward Understanding α-Pinene, The Journal of Physical Chemistry A, 119, 4633-4650, 10.1021/jp510966g, 2015.

570 Riva, M., Heikkinen, L., Bell, D. M., Peräkylä, O., Zha, Q., Schallhart, S., Rissanen, M. P., Imre, D., Petäjä, T., Thornton, J. A., Zelenyuk, A., and Ehn, M.: Chemical transformations in monoterpene-derived organic aerosol enhanced by inorganic composition, npj Climate and Atmospheric Science, 2, 2, 10.1038/s41612-018-0058-0, 2019.

Romonosky, D. E., Li, Y., Shiraiwa, M., Laskin, A., Laskin, J., and Nizkorodov, S. A.: Aqueous Photochemistry of Secondary Organic Aerosol of α-Pinene and α-Humulene Oxidized with Ozone, Hydroxyl Radical, and Nitrate Radical, The Journal of Physical Chemistry A, 121, 1298-1309, 10.1021/acs.jpca.6b10900, 2017.

575 Saunders, S. M., Jenkin, M. E., Derwent, R. G., and Pilling, M. J.: Protocol for the development of the Master Chemical Mechanism, MCM v3 (Part A): tropospheric degradation of non-aromatic volatile organic compounds, Atmos. Chem. Phys., 3, 161-180, 10.5194/acp-3-161-2003, 2003.

Simon, M., Dada, L., Heinritzi, M., Scholz, W., Stolzenburg, D., Fischer, L., Wagner, A. C., Kürten, A., Rörup, B., He, X. C., Almeida, J., Baalbaki, R., Baccarini, A., Bauer, P. S., Beck, L., Bergen, A., Bianchi, F., Bräkling, S., Brilke, S., Caudillo, L., Chen, D., Chu, B., Dias, 580 A., Draper, D. C., Duplissy, J., El Haddad, I., Finkenzeller, H., Frege, C., Gonzalez-Carracedo, L., Gordon, H., Granzin, M., Hakala, J., Hofbauer, V., Hoyle, C. R., Kim, C., Kong, W., Lamkaddam, H., Lee, C. P., Lehtipalo, K., Leiminger, M., Mai, H., Manninen, H. E., Marie, G., Marten, R., Mentler, B., Molteni, U., Nichman, L., Nie, W., Ojdanic, A., Onnela, A., Partoll, E., Petäjä, T., Pfeifer, J., Philippov, M., Quéléver, L. L. J., Ranjithkumar, A., Rissanen, M., Schallhart, S., Schobesberger, S., Schuchmann, S., Shen, J., Sipilä, M., Steiner, G., Stozhkov, Y., Tauber, C., Tham, Y. J., Tomé, A. R., Vazquez-Pufleau, M., Vogel, A., Wagner, R., Wang, M., Wang, D. S., Wang, Y., 585 Weber, S. K., Wu, Y., Xiao, M., Yan, C., Ye, P., Ye, Q., Zauner-Wieczorek, M., Zhou, X., Baltensperger, U., Dommen, J., Flagan, R. C., Hansel, A., Kulmala, M., Volkamer, R., Winkler, P. M., Worsnop, D. R., Donahue, N. M., Kirkby, J., and Curtius, J.: Molecular understanding of new-particle formation from alpha-pinene between -50 °C and 25 °C, Atmos. Chem. Phys. Discuss., 2020, 1-42, 10.5194/acp-2019-1058, 2020.

Stefenelli, G., Pospisilova, V., Lopez-Hilfiker, F. D., Daellenbach, K. R., Hüglin, C., Tong, Y., Baltensperger, U., Prévôt, A. S. H., and 590 Slowik, J. G.: Organic aerosol source apportionment in Zurich using an extractive electrospray ionization time-of-flight mass spectrometer (EESI-TOF-MS) – Part 1: Biogenic influences and day–night chemistry in summer, Atmos. Chem. Phys., 19, 14825-14848, 10.5194/acp-19-14825-2019, 2019.

Surdu, M., Pospisilova, V., Xiao, M., Wang, M., Mentler, B., Simon, M., Stolzenburg, D., Hoyle, C. R., Bell, D. M., Lee, C. P., Lamkaddam, H., Lopez-Hilfiker, F., Ahonen, L. R., Amorim, A., Baccarini, A., Chen, D., Dada, L., Duplissy, J., Finkenzeller, H., He, X.-C., Hofbauer, 595 V., Kim, C., Kürten, A., Kvashnin, A., Lehtipalo, K., Makhmutov, V., Molteni, U., Nie, W., Onnela, A., Petäjä, T., Quéléver, L. L. J., Tauber, C., Tomé, A., Wagner, R., Yan, C., Prevot, A. S. H., Dommen, J., Donahue, N. M., Hansel, A., Curtius, J., Winkler, P. M., Kulmala, M., Volkamer, R., Flagan, R. C., Kirkby, J., Worsnop, D. R., Slowik, J. G., Wang, D. S., Baltensperger, U., and Haddad, I. e.: Molecular characterization of ultrafine particles using extractive electrospray time-of-flight mass spectrometry, Environmental Science: Atmospheres, 10.1039/D1EA00050K, 2021.

600 Takeuchi, M., and Ng, N. L.: Chemical composition and hydrolysis of organic nitrate aerosol formed from hydroxyl and nitrate radical oxidation of α-pinene and β-pinene, Atmos. Chem. Phys., 19, 12749-12766, 10.5194/acp-19-12749-2019, 2019.

Wang, D. S., Lee, C. P., Krechmer, J. E., Majluf, F., Tong, Y., Canagaratna, M. R., Schmale, J., Prévôt, A. S. H., Baltensperger, U., Dommen, J., El Haddad, I., Slowik, J. G., and Bell, D. M.: Constraining the response factors of an extractive electrospray ionization mass spectrometer for near-molecular aerosol speciation, Atmos. Meas. Tech. Discuss., 2021, 1-24, 10.5194/amt-2021-125, 2021.

605 Wolfe, G. M., Marvin, M. R., Roberts, S. J., Travis, K. R., and Liao, J.: The Framework for 0-D Atmospheric Modeling (F0AM) v3.1, Geosci. Model Dev., 9, 3309-3319, 10.5194/gmd-9-3309-2016, 2016.

Wu, C., Bell, D. M., Graham, E. L., Haslett, S., Riipinen, I., Baltensperger, U., Bertrand, A., Giannoukos, S., Schoonbaert, J., El Haddad, I., Prevot, A. S. H., Huang, W., and Mohr, C.: Photolytically Induced Changes in Composition and Volatility of Biogenic Secondary Organic Aerosol from Nitrate Radical Oxidation, Atmos. Chem. Phys., submitted, 2021.

610 Xu, L., Kollman, M. S., Song, C., Shilling, J. E., and Ng, N. L.: Effects of NOx on the Volatility of Secondary Organic Aerosol from Isoprene Photooxidation, Environmental Science & Technology, 48, 2253-2262, 10.1021/es404842g, 2014.

Xu, L., Suresh, S., Guo, H., Weber, R. J., and Ng, N. L.: Aerosol characterization over the southeastern United States using high-resolution aerosol mass spectrometry: spatial and seasonal variation of aerosol composition and sources with a focus on organic nitrates, Atmos. Chem. Phys., 15, 7307-7336, 10.5194/acp-15-7307-2015, 2015.

615 Yan, C., Nie, W., Äijälä, M., Rissanen, M. P., Canagaratna, M. R., Massoli, P., Junninen, H., Jokinen, T., Sarnela, N., Häme, S. A. K., Schobesberger, S., Canonaco, F., Yao, L., Prévôt, A. S. H., Petäjä, T., Kulmala, M., Sipilä, M., Worsnop, D. R., and Ehn, M.: Source characterization of highly oxidized multifunctional compounds in a boreal forest environment using positive matrix factorization, Atmos. Chem. Phys., 16, 12715-12731, 10.5194/acp-16-12715-2016, 2016.

Zhao, D., Pullinen, I., Fuchs, H., Schrade, S., Wu, R., Acir, I. H., Tillmann, R., Rohrer, F., Wildt, J., Guo, Y., Kiendler-Scharr, A., Wahner, 620 A., Kang, S., Vereecken, L., and Mentel, T. F.: Highly oxygenated organic molecules (HOM) formation in the isoprene oxidation by NO3 radical, Atmos. Chem. Phys. Discuss., 2020, 1-28, 10.5194/acp-2020-1178, 2020.

Zhao, Y., Thornton, J. A., and Pye, H. O. T.: Quantitative constraints on autoxidation and dimer formation from direct probing of monoterpene-derived peroxy radical chemistry, Proceedings of the National Academy of Sciences, 115, 12142, 10.1073/pnas.1812147115, 2018.

625 Ziemann, P. J., and Atkinson, R.: Kinetics, products, and mechanisms of secondary organic aerosol formation, Chemical Society Reviews, 41, 6582-6605, 10.1039/C2CS35122F, 2012.
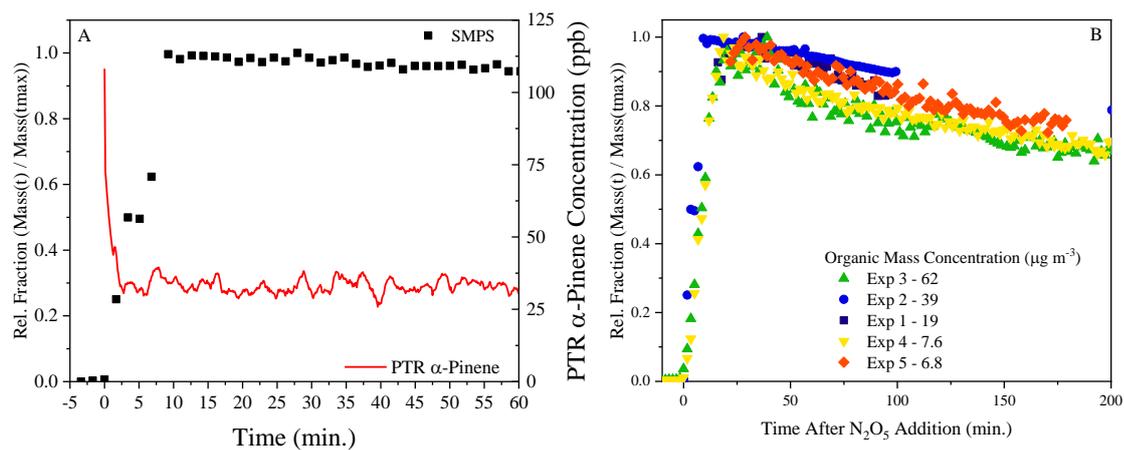
630 **Figure 1:** Evolution of precursor and SOA mass. **(a)** Example from experiment 2 showing prompt SOA formation and consumption of α-pinene. **(b)** All experiments performed showing the evaporation occurring during dark aging as measured by the SMPS, with the organic aerosol mass concentration associated with each experiment.
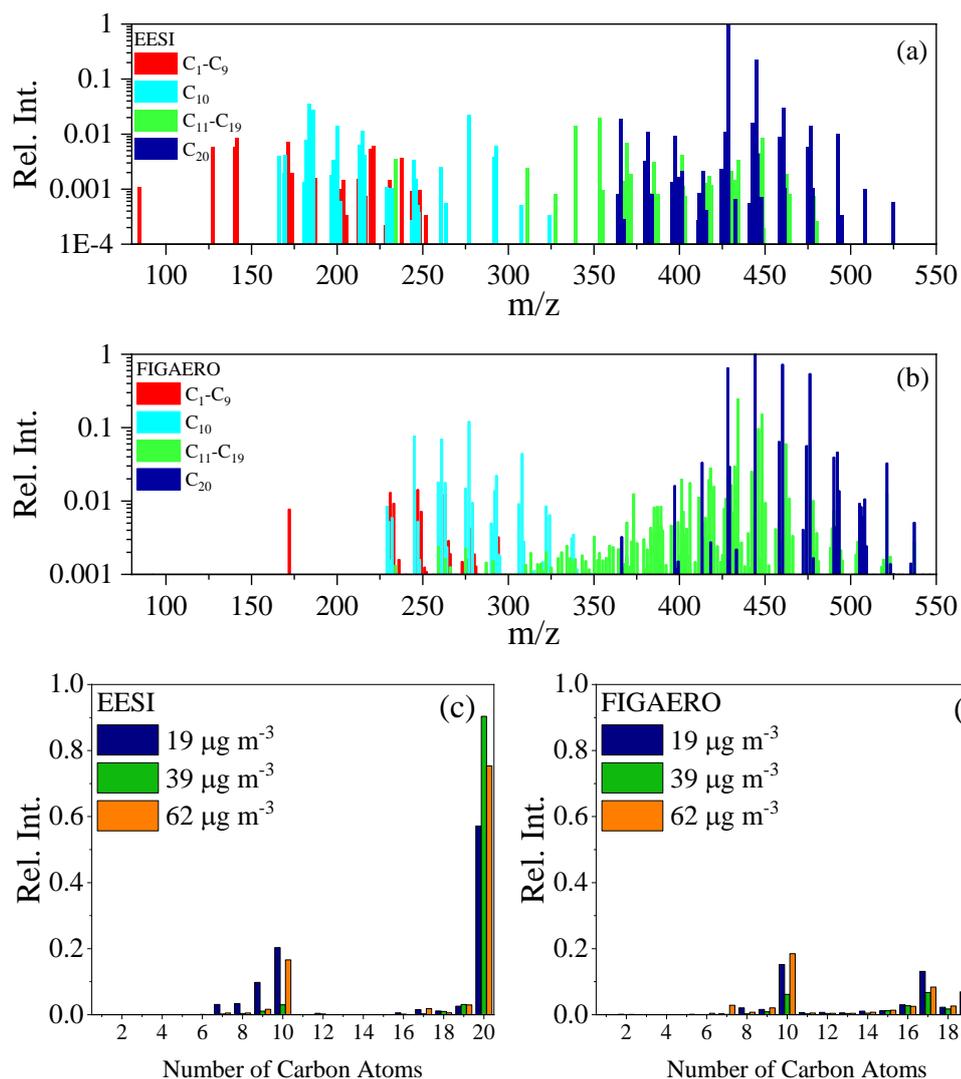
635 **Figure 2**: (**a**) Average mass spectrum presented for the EESI-ToF. (**b**) the first 20 min and FIGAERO-CIMS from the first

desorption from experiments 1 (blue), 2 (green), 3 (orange), respectively, taking place between the first 10-46 min of the

experiment. The main set of molecules correspond to $C_{20}H_{32}N_2O_x$ (x = 8 – 13) for both instruments. (**c & d**) Binned carbon

distribution for experiments 1 – 3 for the same time period for the EESI-ToF and FIGAERO, respectively.

640
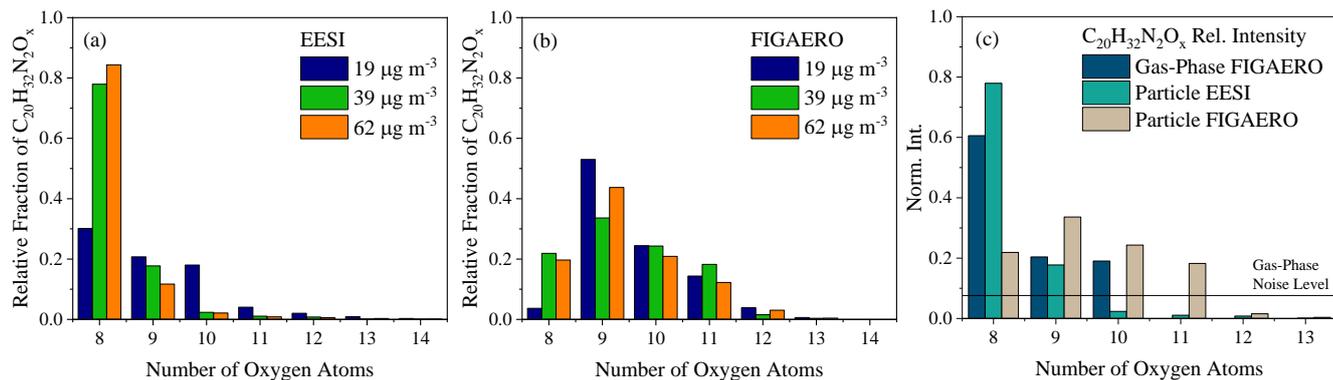
Figure 3: (a & b) Oxygen atom distribution for $C_{20}H_{32}N_2O_{8-14}$ molecules observed by both the EESI-ToF and FIGAERO-CIMS, respectively, experiments 1 (blue), 2 (green), 3 (orange), normalized to the total $C_{20}H_{32}N_2O_x$ signal. The EESI-ToF data is averaged over the first 10 min of the experiments while the FIGAERO-CIMS data represents the first filter desorption. **(c)** Oxygen atom distribution for the FIGAERO-CIMS (gas phase) averaged over the first ~5 min from experiment 2. The solid line denotes the limit of detection for the FIGAERO-CIMS.
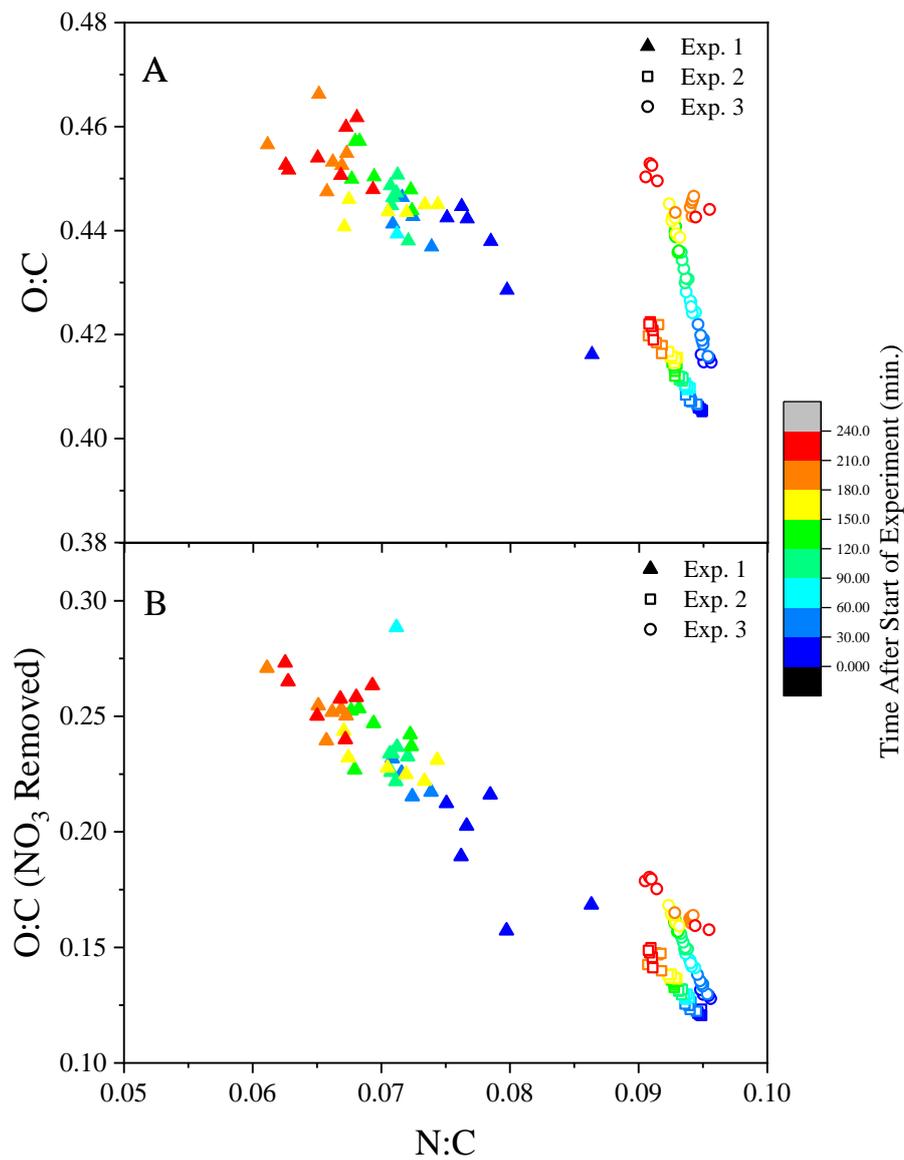
650

Figure 4: (a) N:C and O:C ratios measured by the EESI-ToF over the course of the experiment (color scale). **(b)** O:C ratio altered by the removal of –ONO$_2$ groups from the O:C ratio where #O$_{non-NO3}$ = #O$_{total}$ – 3*#N.
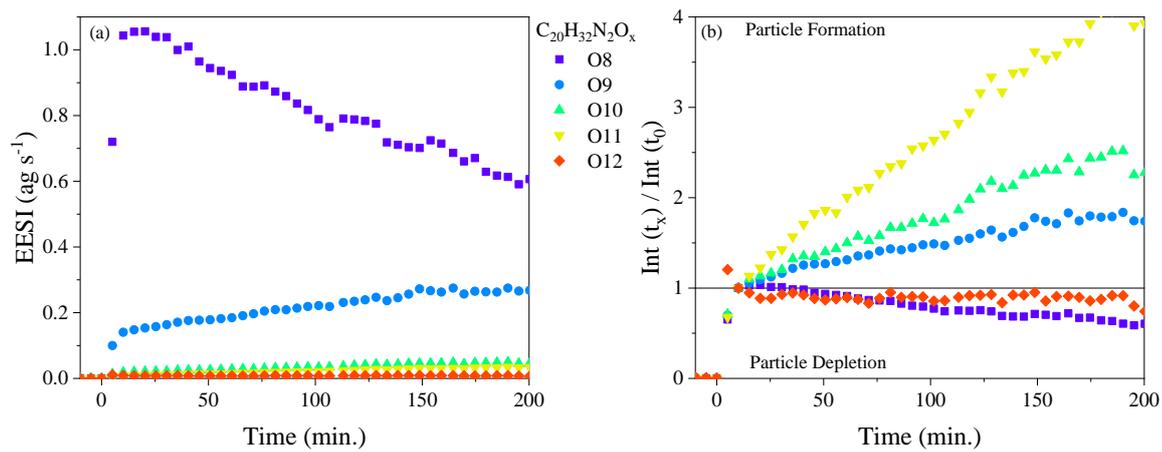
Figure 5: (a) Wall-loss corrected time series of the $C_{20}H_{32}N_2O_{8-13}$ molecules observed by the EESI-ToF over the course of dark aging in the chamber from exp 2. **(b)** All signals normalized to their intensity at $t = 10$ min.
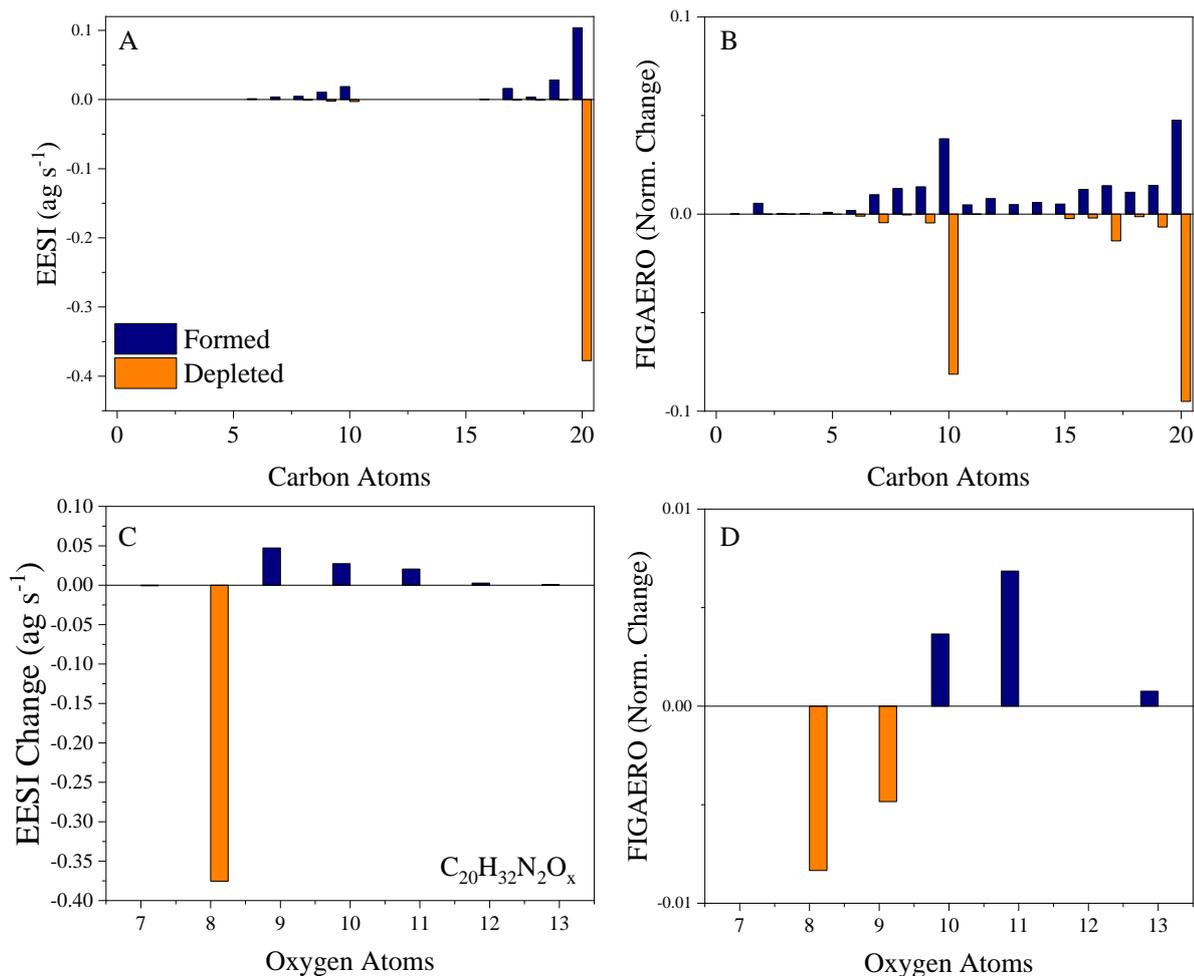
Figure 6: (a & b) Carbon distribution of the molecules formed (blue) and depleted (orange) in the particle phase during aging for both the EESI-ToF **(a)** and FIGAERO-CIMS **(b)**, respectively for exp 3. (**c & d**) The change in the oxygen distribution for the $C_{20}H_{32}N_2O_{8-13}$ molecules during dark aging for the EESI-ToF **(c)** and FIGAERO-CIMS **(d)**, respectively. For panels A and C , a difference is obtained by taking the difference from $t = 15$ min and $t = 150$ min from the EESI-ToF. Panels B and D are obtained by taking the difference in the relative sensitivity from the 1st and 3rd filter. For all figures, the formation is shifted negative on the x-axis relative to the nominal carbon number, and the depletion is shifted positive on the x-axis comparatively.
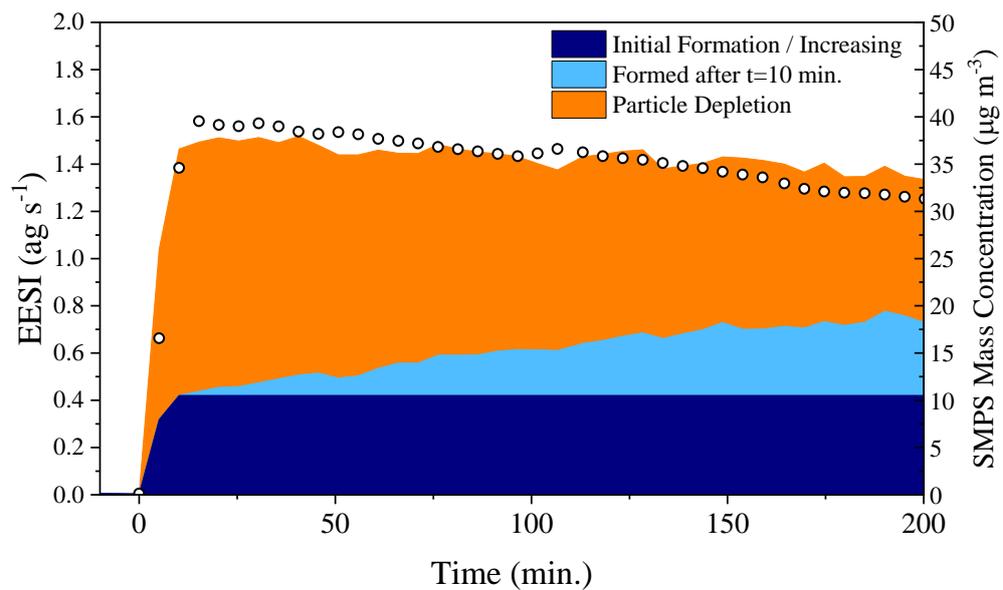
Figure 7: (left axis) Total EESI-ToF intensity plotted as a function of the contribution from different sources, particle phase formation products determined from those molecular formulae that increase during dark aging after $t = 10$ min from experiment 2. **(right axis)** Measured SMPS mass concentration corrected for wall losses.